DESY 97-210 ISSN 04118-9833

Thrust Jet Analysis of Deep–Inelastic Large–Rapidity–Gap Events

H1 Collaboration

Abstract

A thrust analysis of Large-Rapidity-Gap events in deep-inelastic *ep* collisions is presented, using data taken with the H1 detector at HERA in 1994. The average thrust of the final states X, which emerge from the dissociation of virtual photons in the range $10 < Q^2 < 100$ GeV^2, grows with hadronic mass M_X and implies a dominant 2-jet topology. Thrust is found to decrease with growing P_t, the thrust jet momentum transverse to the photon-proton collision axis. Distributions of P_t^2 are consistent with being independent of M_X. They show a strong alignment of the thrust axis with the photon-proton collision axis, and have a large high$-P_t$ tail. The correlation of thrust with M_X is similar to that in e^+e^- annihilation at $\sqrt{s}_{ee} = M_X$, but with lower values of thrust in the *ep* data. The data cannot be described by interpreting the dissociated system X as a $q\bar{q}$ state but inclusion of a substantial fraction of $q\bar{q}g$ parton configurations leads naturally to the observed properties. The soft colour exchange interaction model does not describe the data.

To be submitted to Zeitschrift für Physik ***C***

H1 Collaboration

C. Adloff[35], S. Aid[13], M. Anderson[23], V. Andreev[26], B. Andrieu[29], V. Arkadov[36], C. Arndt[11], I. Ayyaz[30], A. Babaev[25], J. Bähr[36], J. Bán[18], P. Baranov[26], E. Barrelet[30], R. Barschke[11], W. Bartel[11], U. Bassler[30], M. Beck[14], H.-J. Behrend[11], C. Beier[16], A. Belousov[26], Ch. Berger[1], G. Bernardi[30], G. Bertrand-Coremans[4], R. Beyer[11], P. Biddulph[23], J.C. Bizot[28], K. Borras[8], F. Botterweck[27], V. Boudry[29], S. Bourov[25], A. Braemer[15], W. Braunschweig[1], V. Brisson[28], D.P. Brown[23], W. Brückner[14], P. Bruel[29], D. Bruncko[18], C. Brune[16], J. Bürger[11], F.W. Büsser[13], A. Buniatian[4], S. Burke[19], G. Buschhorn[27], D. Calvet[24], A.J. Campbell[11], T. Carli[27], M. Charlet[11], D. Clarke[5], B. Clerbaux[4], S. Cocks[20], J.G. Contreras[8], C. Cormack[20], J.A. Coughlan[5], M.-C. Cousinou[24], B.E. Cox[23], G. Cozzika[9], D.G. Cussans[5], J. Cvach[31], S. Dagoret[30], J.B. Dainton[20], W.D. Dau[17], K. Daum[40], M. David[9], C.L. Davis[19,41], A. De Roeck[11], E.A. De Wolf[4], B. Delcourt[28], M. Dirkmann[8], P. Dixon[19], W. Dlugosz[7], K.T. Donovan[21], J.D. Dowell[3], A. Droutskoi[25], J. Ebert[35], T.R. Ebert[20], G. Eckerlin[11], V. Efremenko[25], S. Egli[38], R. Eichler[37], F. Eisele[15], E. Eisenhandler[21], E. Elsen[11], M. Erdmann[15], A.B. Fahr[13], L. Favart[28], A. Fedotov[25], R. Felst[11], J. Feltesse[9], J. Ferencei[18], F. Ferrarotto[33], K. Flamm[11], M. Fleischer[8], M. Flieser[27], G. Flügge[2], A. Fomenko[26], J. Formánek[32], J.M. Foster[23], G. Franke[11], E. Gabathuler[20], K. Gabathuler[34], F. Gaede[27], J. Garvey[3], J. Gayler[11], M. Gebauer[36], R. Gerhards[11], A. Glazov[36], L. Goerlich[6], N. Gogitidze[26], M. Goldberg[30], B. Gonzalez-Pineiro[30], I. Gorelov[25], C. Grab[37], H. Grässler[2], T. Greenshaw[20], R.K. Griffiths[21], G. Grindhammer[27], A. Gruber[27], C. Gruber[17], T. Hadig[1], D. Haidt[11], L. Hajduk[6], T. Haller[14], M. Hampel[1], W.J. Haynes[5], B. Heinemann[11], G. Heinzelmann[13], R.C.W. Henderson[19], S. Hengstmann[38], H. Henschel[36], I. Herynek[31], M.F. Hess[27], K. Hewitt[3], K.H. Hiller[36], C.D. Hilton[23], J. Hladký[31], M. Höppner[8], D. Hoffmann[11], T. Holtom[20], R. Horisberger[34], V.L. Hudgson[3], M. Hütte[8], M. Ibbotson[23], Ç. İşsever[8], H. Itterbeck[1], M. Jacquet[28], M. Jaffre[28], J. Janoth[16], D.M. Jansen[14], L. Jönsson[22], D.P. Johnson[4], H. Jung[22], P.I.P. Kalmus[21], M. Kander[11], D. Kant[21], U. Kathage[17], J. Katzy[15], H.H. Kaufmann[36], O. Kaufmann[15], M. Kausch[11], S. Kazarian[11], I.R. Kenyon[3], S. Kermiche[24], C. Keuker[1], C. Kiesling[27], M. Klein[36], C. Kleinwort[11], G. Knies[11], J.H. Köhne[27], H. Kolanoski[39], S.D. Kolya[23], V. Korbel[11], P. Kostka[36], S.K. Kotelnikov[26], T. Krämerkämper[8], M.W. Krasny[6,30], H. Krehbiel[11], D. Krücker[27], A. Küpper[35], H. Küster[22], M. Kuhlen[27], T. Kurča[36], B. Laforge[9], R. Lahmann[11], M.P.J. Landon[21], W. Lange[36], U. Langenegger[37], A. Lebedev[26], F. Lehner[11], V. Lemaitre[11], S. Levonian[29], M. Lindstroem[22], J. Lipinski[11], B. List[11], G. Lobo[28], G.C. Lopez[12], V. Lubimov[25], D. Lüke[8,11], L. Lytkin[14], N. Magnussen[35], H. Mahlke-Krüger[11], E. Malinovski[26], R. Maraček[18], P. Marage[4], J. Marks[15], R. Marshall[23], J. Martens[35], G. Martin[13], R. Martin[20], H.-U. Martyn[1], J. Martyniak[6], T. Mavroidis[21], S.J. Maxfield[20], S.J. McMahon[20], A. Mehta[5], K. Meier[16], P. Merkel[11], F. Metlica[14], A. Meyer[13], A. Meyer[11], H. Meyer[35], J. Meyer[11], P.-O. Meyer[2], A. Migliori[29], S. Mikocki[6], D. Milstead[20], J. Moeck[27], F. Moreau[29], J.V. Morris[5], E. Mroczko[6], D. Müller[38], K. Müller[11], P. Murín[18], V. Nagovizin[25], R. Nahnhauer[36], B. Naroska[13], Th. Naumann[36], I. Négri[24], P.R. Newman[3], D. Newton[19], H.K. Nguyen[30], T.C. Nicholls[3], F. Niebergall[13], C. Niebuhr[11], Ch. Niedzballa[1], H. Niggli[37], G. Nowak[6], T. Nunnemann[14], H. Oberlack[27], J.E. Olsson[11], D. Ozerov[25], P. Palmen[2], E. Panaro[11], A. Panitch[4], C. Pascaud[28], S. Passaggio[37], G.D. Patel[20], H. Pawletta[2], E. Peppel[36], E. Perez[9], J.P. Phillips[20], A. Pieuchot[24], D. Pitzl[37], R. Pöschl[8], G. Pope[7], B. Povh[14], K. Rabbertz[1], P. Reimer[31], H. Rick[8], S. Riess[13], E. Rizvi[11], E. Rizvi[21], P. Robmann[38], R. Roosen[4], K. Rosenbauer[1], A. Rostovtsev[30], F. Rouse[7], C. Royon[9], K. Rüter[27], S. Rusakov[26], K. Rybicki[6], D.P.C. Sankey[5], P. Schacht[27], J. Scheins[1], S. Schiek[11], S. Schleif[16], P. Schleper[15], W. von Schlippe[21], D. Schmidt[35], G. Schmidt[11], L. Schoeffel[9], A. Schöning[11], V. Schröder[11], E. Schuhmann[27], H.-C. Schultz-Coulon[11], B. Schwab[15], F. Sefkow[38], A. Semenov[25], V. Shekelyan[11], I. Sheviakov[26], L.N. Shtarkov[26], G. Siegmon[17], U. Siewert[17], Y. Sirois[29], I.O. Skillicorn[10], T. Sloan[19], P. Smirnov[26], M. Smith[20], V. Solochenko[25], Y. Soloviev[26],

A. Specka[29], J. Spiekermann[8], S. Spielman[29], H. Spitzer[13], F. Squinabol[28], P. Steffen[11], R. Steinberg[2], J. Steinhart[13], B. Stella[33], A. Stellberger[16], J. Stiewe[16], K. Stolze[36], U. Straumann[15], W. Struczinski[2], J.P. Sutton[3], M. Swart[16], S. Tapprogge[16], M. Taševský[32], V. Tchernyshov[25], S. Tchetchelnitski[25], J. Theissen[2], G. Thompson[21], P.D. Thompson[3], N. Tobien[11], R. Todenhagen[14], P. Truöl[38], J. Zálešák[32], G. Tsipolitis[37], J. Turnau[6], E. Tzamariudaki[11], P. Uelkes[2], A. Usik[26], S. Valkár[32], A. Valkárová[32], C. Vallée[24], P. Van Esch[4], P. Van Mechelen[4], D. Vandenplas[29], Y. Vazdik[26], P. Verrecchia[9], G. Villet[9], K. Wacker[8], A. Wagener[2], M. Wagener[34], R. Wallny[15], T. Walter[38], B. Waugh[23], G. Weber[13], M. Weber[16], D. Wegener[8], A. Wegner[27], T. Wengler[15], M. Werner[15], L.R. West[3], S. Wiesand[35], T. Wilksen[11], S. Willard[7], M. Winde[36], G.-G. Winter[11], C. Wittek[13], M. Wobisch[2], H. Wollatz[11], E. Wünsch[11], J. Žáček[32], D. Zarbock[12], Z. Zhang[28], A. Zhokin[25], P. Zini[30], F. Zomer[28], J. Zsembery[9], and M. zurNedden[38],

[1] I. Physikalisches Institut der RWTH, Aachen, Germany[a]
[2] III. Physikalisches Institut der RWTH, Aachen, Germany[a]
[3] School of Physics and Space Research, University of Birmingham, Birmingham, UK[b]
[4] Inter-University Institute for High Energies ULB-VUB, Brussels; Universitaire Instelling Antwerpen, Wilrijk; Belgium[c]
[5] Rutherford Appleton Laboratory, Chilton, Didcot, UK[b]
[6] Institute for Nuclear Physics, Cracow, Poland[d]
[7] Physics Department and IIRPA, University of California, Davis, California, USA[e]
[8] Institut für Physik, Universität Dortmund, Dortmund, Germany[a]
[9] DSM/DAPNIA, CEA/Saclay, Gif-sur-Yvette, France
[10] Department of Physics and Astronomy, University of Glasgow, Glasgow, UK[b]
[11] DESY, Hamburg, Germany[a]
[12] I. Institut für Experimentalphysik, Universität Hamburg, Hamburg, Germany[a]
[13] II. Institut für Experimentalphysik, Universität Hamburg, Hamburg, Germany[a]
[14] Max-Planck-Institut für Kernphysik, Heidelberg, Germany[a]
[15] Physikalisches Institut, Universität Heidelberg, Heidelberg, Germany[a]
[16] Institut für Hochenergiephysik, Universität Heidelberg, Heidelberg, Germany[a]
[17] Institut für Reine und Angewandte Kernphysik, Universität Kiel, Kiel, Germany[a]
[18] Institute of Experimental Physics, Slovak Academy of Sciences, Košice, Slovak Republic[f,j]
[19] School of Physics and Chemistry, University of Lancaster, Lancaster, UK[b]
[20] Department of Physics, University of Liverpool, Liverpool, UK[b]
[21] Queen Mary and Westfield College, London, UK[b]
[22] Physics Department, University of Lund, Lund, Sweden[g]
[23] Physics Department, University of Manchester, Manchester, UK[b]
[24] CPPM, Université d'Aix-Marseille II, IN2P3-CNRS, Marseille, France
[25] Institute for Theoretical and Experimental Physics, Moscow, Russia
[26] Lebedev Physical Institute, Moscow, Russia[f]
[27] Max-Planck-Institut für Physik, München, Germany[a]
[28] LAL, Université de Paris-Sud, IN2P3-CNRS, Orsay, France
[29] LPNHE, Ecole Polytechnique, IN2P3-CNRS, Palaiseau, France
[30] LPNHE, Universités Paris VI and VII, IN2P3-CNRS, Paris, France
[31] Institute of Physics, Czech Academy of Sciences of the Czech Republic, Praha, Czech Republic[f,h]
[32] Nuclear Center, Charles University, Praha, Czech Republic[f,h]
[33] INFN Roma 1 and Dipartimento di Fisica, Università Roma 3, Roma, Italy
[34] Paul Scherrer Institut, Villigen, Switzerland
[35] Fachbereich Physik, Bergische Universität Gesamthochschule Wuppertal, Wuppertal, Germany[a]
[36] DESY, Institut für Hochenergiephysik, Zeuthen, Germany[a]
[37] Institut für Teilchenphysik, ETH, Zürich, Switzerland[i]
[38] Physik-Institut der Universität Zürich, Zürich, Switzerland[i]
[39] Institut für Physik, Humboldt-Universität, Berlin, Germany[a]
[40] Rechenzentrum, Bergische Universität Gesamthochschule Wuppertal, Wuppertal, Germany[a]

[a] Supported by the Bundesministerium für Bildung, Wissenschaft, Forschung und Technologie, FRG, under contract numbers 6AC17P, 6AC47P, 6DO57I, 6HH17P, 6HH27I, 6HD17I, 6HD27I, 6KI17P, 6MP17I, and 6WT87P

[b] Supported by the UK Particle Physics and Astronomy Research Council, and formerly by the UK Science and Engineering Research Council

[c] Supported by FNRS-NFWO, IISN-IIKW

[d] Partially supported by the Polish State Committee for Scientific Research, grant no. 115/E-343/SPUB/P03/120/96

[e] Supported in part by USDOE grant DE F603 91ER40674

[f] Supported by the Deutsche Forschungsgemeinschaft

[g] Supported by the Swedish Natural Science Research Council

[h] Supported by GA ČR grant no. 202/96/0214, GA AV ČR grant no. A1010619 and GA UK grant no. 177

[i] Supported by the Swiss National Science Foundation

[j] Supported by VEGA SR grant no. 2/1325/96

1 Introduction

The Large-Rapidity-Gap (LRG) events observed at the ep collider HERA [1, 2] are attributed mainly to diffraction [3, 4]. The kinematics of these events can be discussed quite generally in terms of the process $ep \to e'XY$ (see Fig. 1), where the two hadronic systems X and Y are

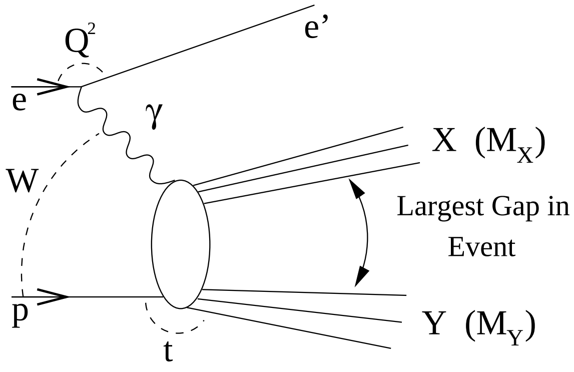

Figure 1: Illustration of the process, $ep \to e'XY$, in which the hadron systems X and Y are separated by the largest rapidity gap in the event. W is the invariant mass of the colliding virtual photon - beam proton system. $-Q^2$ is the square of the 4-momentum transfer at the (e, e') vertex, and t at the (p, Y) vertex. M_X and M_Y are the masses of systems X and Y, respectively.

separated by the largest rapidity gap in the event. In the H1 experiment, events are selected with no activity over a particular large pseudorapidity range adjacent to the outgoing proton beam (forward) direction. In these events the system Y remains as a proton, or is excited to a low mass baryonic system by a colourless exchange with a small transverse component in the momentum transfer [1] $I\!P = p - Y$. The incoming photon, ranging from very low to high virtuality Q^2, can be excited [5] into a vector meson ($\gamma^{(*)} + p \to V + Y$), or can dissociate into a high mass state X ($\gamma^{(*)} + p \to X + Y$).

In this paper, the topological structure of final states, which emerge from the dissociation of highly virtual photons, is investigated. In the photon dissociation (PD) picture this process can be related to the fluctuation of the virtual photon into partonic states [6, 7, 8, 9], followed by parton-proton quasi-elastic diffractive scattering, as shown in Fig. 2. In the proton infinite momentum frame (IMF) picture the diagrams [2] in Fig. 2 can also be described in terms of deep-inelastic scattering (DIS) off an exchanged object with partonic content [10, 3, 4].

The simplest PD process was first discussed by Bjorken and Kogut [6], in terms of the quark-parton model in the form of the Aligned Jet Model (AJM). Here the photon fluctuates into a quark anti-quark pair long before it actually collides with the proton.

Quark anti-quark ($q\bar{q}$) configurations with large parton momenta k_t transverse to the collision axis are predicted to have a reduced cross section in comparison with the expectation for a hypothetical collision of two single quarks with the proton. This suppression of large k_t has been explained in terms of "colour transparency" [11], since the physical transverse separation of the $q\bar{q}$ state is small on average, leading to a small colour dipole moment, or equivalently to mutual screening. However, $q\bar{q}$ configurations with a small transverse momentum difference

[1] Here, and throughout this paper, the term pomeron and the symbol $I\!P$ are used for the colourless exchanged object independently of its nature, unless the difference between a pomeron and a subleading reggeon exchange is significant in the context.

[2] The names for the respective processes as given in the caption are appropriate for the IMF interpretation of these diagrams. Because the two interpretations of the diagrams in Fig. 2 are equivalent, these names are used also when referring to each of Fig 2a through 2d in the PD interpretation.

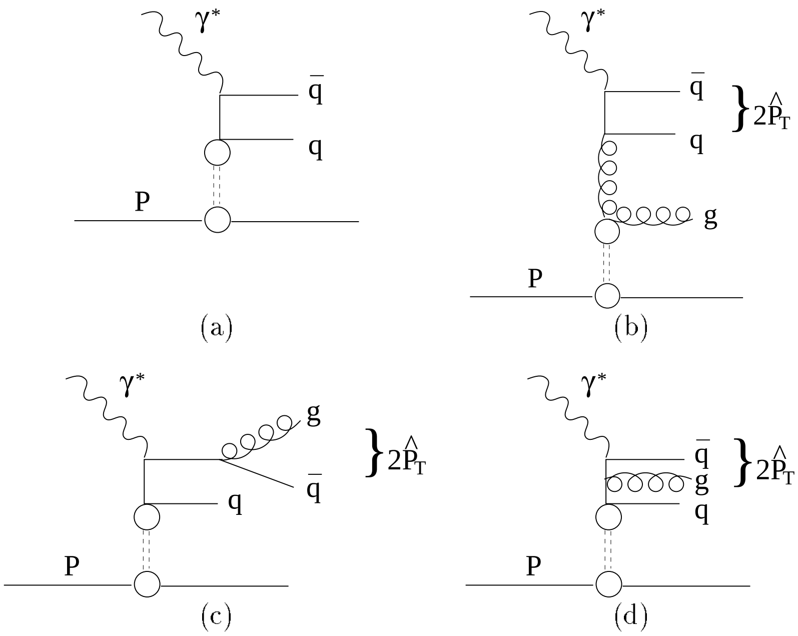

Figure 2: Diagrams of parton processes for LRG events: Born term diagram (a), boson-gluon fusion (BGF) (b), QCD-Compton (QCD-C) (c, d). The $q \leftrightarrow \bar{q}$ exchanged configurations are implied.

do not lead to such screening effects and hence are not suppressed in their interaction with the proton. In the rest frame of X, the AJM picture thus leads to a back-to-back 2-jet configuration with small jet transverse momenta P_t relative to the incoming proton beam direction, typical of soft interactions.

The QCD extension of this simple AJM model with gluons radiated by the $q\bar{q}$ system was proposed in [12], and has been studied further by several authors [7], in particular by invoking a soft colour interaction (SCI) process [8, 9]. In the IMF view this corresponds to a QCD evolution of the structure function of the diffractive exchange.

Two further and completely different approaches have been used to explain LRG event production. In one of them the LRG events are the result of normal DIS scattering with a subsequent SCI process [13], generating a large rapidity gap. In the other one it is proposed that the virtual photon fluctuates according to the Generalized Vector Meson Dominance Model (GVDM) [14] into virtual vector mesons which then undergo diffractive scattering off the proton [15, 16].

All the above approaches are phenomenological and one can alter parameters to describe the inclusive production cross section for LRG events. They lead, however, to distinctive features in the topology of the hadronic final state.

Topological studies were essential in analysing the transition of timelike photons into partons in e^+e^- annihilation, even at energies $\sqrt{s_{ee}}$ which were too low to resolve 3-jet from 2-jet events [17]. The contribution of higher order parton configurations like $q\bar{q}g$, relative to $q\bar{q}$, was determined without applying jet algorithms, by measuring the deviation from collinear momentum flow using the event-shape variable thrust T [18, 19]. Data on the evolution of thrust with $\sqrt{s_{ee}}$ also allowed a separation of hadronization from perturbative QCD effects to be made.

In this analysis, thrust is used to study topological features of the hadronic final state in γ^* dissociation in a kinematic regime where diffractive contributions are dominant [20]. Here the final state partonic structure and the related hadronization effects may be different from those in e^+e^- annihilation events. The correlation of thrust with M_X may be exploited to separate these two contributions. In addition, the alignment, i.e. the correlation of the thrust direction with the incoming proton direction, can be investigated by studying the P_t distribution of thrust jets with respect to the proton direction and can be used as a further tool for the analysis of the dynamics of LRG events.

Because of a forward rapidity gap requirement, the hadronic final states of accepted events are well contained in the central detectors of H1. This provides measurement conditions similar to those in e^+e^- annihilation experiments at symmetric e^+e^- colliders. No jet energy threshold is required in the thrust analysis and all events in the M_X range under study are included. An event shape analysis of LRG events has been reported recently by the ZEUS collaboration [21].

2 Detector description

In the following, only detector components relevant for this analysis are reviewed. A detailed description of the H1 detector can be found elsewhere [22].

The "backward" electromagnetic calorimeter (BEMC) has full azimuthal coverage, and extends over the range $151^\circ < \theta < 176^\circ$, where θ is the polar angle with respect to the proton beam direction, as seen from the nominal beam collision point. The BEMC was used to trigger on and measure the energy of the scattered electron in DIS processes. The electromagnetic energy resolution is $\sigma_E/E = 0.10/\sqrt{E\,[\mathrm{GeV}]} \oplus 0.42/E[\,\mathrm{GeV}\,] \oplus 0.03$ [23], while the absolute electromagnetic energy scale is known with an accuracy of 1%. The BEMC hadronic energy scale is known to a precision of 20%. The backward proportional chamber (BPC), located in front of the BEMC detector, has an acceptance of $155.5^\circ < \theta < 174.5^\circ$ and, in conjunction with the interaction vertex, measures the direction of the scattered electron with a precision of 1 mrad. These "backward" detectors accept DIS processes with Q^2 values ranging from 5 to 120 GeV^2. The liquid argon (LAr) calorimeter extends over the polar angular range $4^\circ < \theta < 154^\circ$ with full azimuthal coverage. The electromagnetic energy resolution is $\sigma_E/E \approx 0.11/\sqrt{E\,[\mathrm{GeV}]} \oplus 0.01$, while the hadronic energy resolution is $\sigma_E/E \approx 0.50/\sqrt{E\,[\mathrm{GeV}]} \oplus 0.02$ as determined in test beams. A study of the transverse momentum balance between the hadronic final state and the scattered electron, $P_{t,h} - P_{t,e'}$, has shown that the absolute hadronic energy scale is known to an accuracy of 4%.

The LAr calorimeter is surrounded by a superconducting solenoid providing a uniform magnetic field of 1.15 T parallel to the beam axis in the tracking region. The track reconstruction is based on the information from the central jet chamber (CJC), the z-drift chambers and the forward tracker. These detectors cover a polar angular range of $5^\circ < \theta < 155^\circ$.

Forward energy deposits at small angles are observed in several detectors near the outgoing proton beam direction. Particles reach these detectors both directly from the interaction point, and indirectly as a result of secondary scattering with the beam pipe wall or adjacent material such as collimators. These detectors are thus sensitive to particles well outside their nominal geometrical acceptances. The liquid argon calorimeter is sensitive to particles with pseudorapidities $\eta = -\ln\tan\theta/2$ up to $\eta \simeq 5.5$. A copper-silicon sandwich calorimeter (PLUG) allows energy measurements to be made over the range $3.5 < \eta < 5.5$. The three double layers of drift chambers of the forward muon detector (FMD) are sensitive to particles produced at pseudorapidities $5.0 < \eta < 6.5$. The proton remnant tagger (PRT), consisting of seven double layers of lead/scintillators, located 24 m from the interaction point, covers the region $6.0 < \eta < 7.5$.

These detectors overlap considerably in their rapidity coverage, thereby allowing intercalibration of their efficiencies.

3 Physics models for LRG event production

In the PD picture the photon fluctuates into a $q\bar{q}$, $q\bar{q}g$, or states with more partons, where at least one of the partons is virtual. A virtual parton, if it has a low k_t relative to the $\gamma^* p$ collision axis, can scatter diffractively (quasi-elastically) with the proton yielding a real parton. In the $q\bar{q}$ configuration (Fig. 2a) this gives an aligned 2-jet event, and at least one aligned jet in the 3-parton configurations (Figs. 2b, c and d). It is expected qualitatively that the $q\bar{q}g$ configuration has a larger cross section than the $q\bar{q}$ configuration for diffractive scattering off the proton [9].

In the IMF picture the diagrams in Fig. 2 are interpreted as the DIS probing a colourless exchange object. This is implemented in the RAPGAP [24] Monte Carlo (MC) program. The RAPGAP model employs deep-inelastic electron scattering off pomerons [10] and off (subleading) reggeons coupling to the proton. The pomeron is ascribed a quark and a gluon content. The ratios of the BGF to the Born term and to the QCD-C contributions (see Fig. 2) depend on the gluon and quark contents of the exchanged objects. These have been determined from a QCD analysis with DGLAP evolution [25] of the diffractive structure function measured by the H1 collaboration [26], with the result that most of the pomeron momentum is carried by gluons. For the reggeon, the quark and gluon content is taken to be that of the pion [27].

The RAPGAP model is used in two modes. The matrix element mode (ME) includes the BGF and the QCD-C processes as first order perturbative QCD (pQCD) matrix elements, with propagators for the parton mediating the hard process, while the diagram in Fig. 2a (Diagram 2a), is treated as DIS off a quark in the pomeron. The ARIADNE [28] mode (AR) also treats the BGF process as a matrix element, but treats Diagrams 2c and 2d as colour dipole radiation from the $q\bar{q}$ pair of Diagram 2a. A cut-off in terms of the square of the transverse momentum of the hard sub-process, $\hat{p}_t^2 \geq \hat{p}_{t,min}^2 (= 2\ \mathrm{GeV}^2)$ is applied to keep the contribution from diagrams treated as pQCD matrix elements below the measured total cross section at each (M_X, Q^2, x) point. With this choice [24] of cut-off, the corresponding diagrams of Fig. 2 contribute about 50% of the total diffractive cross section within RAPGAP. The remainder is generated with the process of Diagram 2a. The cut-off value can be raised, but it cannot be lowered without the need to readjust other parameters influencing the total cross section. The topological properties, like thrust or thrust jet P_t, of the simulated events are sensitive to the fraction of matrix element events and depend on the value chosen for $\hat{p}_{t,min}$.

In the RAPGAP ME mode higher order QCD effects are included by means of leading-log parton showers for all final state partons. Predictions of this mode are labelled as 'RG ME+PS' in the following. In the AR mode higher orders are included as additional gluon radiation according to the Colour Dipole Model [29] (labelled as 'RG AR+CD'). In both modes the hadronization is as given by the Lund string fragmentation model [30].

In generating events corresponding to Diagram 2a the $q\bar{q}$ system is taken to be aligned exactly with the $\gamma^* I\!P$ axis, i.e. without intrinsic k_t. The virtuality of the quark mediating the interaction between the photon and the pomeron is thus always taken as the smallest value which is kinematically allowed. These events can be considered as representing the simple AJM, which differs from the RAPGAP simulation of Diagram 2a by having no QCD dipole radiation, and by neglecting transverse momentum transfer to the proton. The corresponding predictions are labelled as 'RG q$\bar{\mathrm{q}}$'.

The non-diffractive ep DIS plus SCI picture is implemented in the LEPTO event generator [31]. This employs the same hard processes as shown in Fig. 2, but now off the proton. The ratio of the generated $q\bar{q}g$ to $q\bar{q}$ events is determined by an infrared cut-off [3] and the parton density functions for the proton. Both are adjusted to describe the total DIS event sample, but

[3] The infrared safety scheme in LEPTO avoids a sharp cut-off in $\hat{p}_t$.

there is no parameter in LEPTO to adjust specifically for the topological properties of the LRG events. This is different from the RAPGAP model where the relative gluon and quark content of the pomeron and the $\hat{p}_{t,min}$ value can be adjusted separately to describe the LRG event data. The parameter which controls the strength of the SCI process has no influence on the topological properties of the system X. The SCI process, and hence the LRG which separates the systems X and Y in Fig. 1, is not limited to occur between the remnant partons of the struck proton and those emerging from the hard process. Thus, the final state X can in general not be identified with a specific hard process.

Predictions from the GVDM picture for final state properties require further specifications of the diffraction process as a hadronic collision.

4 Thrust jet analysis method

In the centre of mass of a system X of N particles, the thrust method determines the direction of the unit vector $\vec{a}$ along which the projected momentum flow is maximal [18]. Thrust is computed as [19]:

$$T = (1/\sum_{i=1}^{N} |\vec{p}_i|) \cdot \max_{\vec{a}} \sum_{i=1}^{N} |\vec{p}_i \cdot \vec{a}|$$

where $\vec{p}_i$ represents the momentum of particle i, in the rest frame of the N particles [4].

Given the thrust axis $\vec{a}$, the directional sense of which is arbitrary, the N particles can then be grouped uniquely into two subsets (thrust jets), depending on whether they belong to the hemisphere with positive or negative momentum component along the thrust axis. The summed particle momenta of hemisphere I form the jet 4-momentum $P_I = \sum_{j=1}^{N_I} p_j$ with N_I the number of particles in hemisphere I, for $I = 1, 2$. The two thrust jets have independent masses, and equal but opposite 3-momenta: $|\vec{P}_{1,2}| = P$.

Thrust values range from a maximum value of $T = 1$ in the case of a 2-particle state or any collinear configuration, to a minimum value of $T = 0.5$ obtained in an isotropic system X with infinite multiplicity. A symmetric 3-particle configuration yields a value $T = 2/3$ and leaves the direction $\vec{a}$ arbitrary in the 3-particle plane, while a non-symmetric topology gives $T > 2/3$ and a thrust axis pointing in the direction of the most energetic particle. A non-symmetric 3-particle topology will thus appear as a 2-jet like configuration with $T < 1$.

In a multihadron state emerging from a partonic process, the two back-to-back reconstructed thrust jets are correlated with the hard partons in the following way. In the case of a 2-parton configuration, the thrust value as determined from the final state hadrons – i.e. at the hadron level – is smaller than 1, and the direction of the thrust axis remains parallel to the direction of the two partons to the extent that the hadrons can be correctly assigned to 'parent-partons'. For an underlying 3-parton system, the reconstructed thrust axis at the hadron level is correlated with the direction of the most energetic parton. This property has been verified to persist down

[4]There is another definition of thrust (T_M) in the literature [19], where the normalization is not to $\sum_{i=1}^{N} |\vec{p}_i|$ as in T but rather to M_X, where M_X is the invariant mass of the system X. If final states contain massive particles, $T_M < T$. To compute T_M accurately, it is necessary to identify all final state particles, which is usually not possible experimentally.

to final state masses $M_X \sim 5$ GeV, using $q\bar{q}g$ events from the RAPGAP event generator [24] with hadronization and detector effects included in the event simulation.

A transverse thrust jet momentum P_t can be defined relative to a reference direction $\vec{r}$ as $P_t = P \cdot \sin\Theta$ with Θ the angle between $\vec{P_i}$ and $\vec{r}$. In this analysis, the proton beam direction transformed into the centre of mass frame of the system X is chosen for $\vec{r}$. Since the 4-momentum transfer squared t is small in LRG events, this direction is a good approximation to the $\gamma^* I\!P$ axis. For $t = t_{min}$ they are identical. Monte Carlo studies have shown that a diffractive $t - t_{min}$ distribution with an exponential slope parameter $b = 6$ GeV^{-2} leads to an average smearing of P_t of less than 0.3 GeV. Unlike the γ^* direction, when calculated from the scattered electron, the proton direction in the X rest frame is not affected by QED-radiation. The $I\!P$ direction is not well determined experimentally.

If events with large thrust jet P_t are dominantly caused by single gluon radiation from an aligned $q\bar{q}$ state, then large P_t will be correlated with lower average thrust $\langle T \rangle$. If the larger P_t values were instead caused by a rotation of a $q\bar{q}$ configuration to larger angles, i.e. by larger intrinsic k_t, then thrust would not change with P_t. Hence, the observation of a decrease of $\langle T \rangle$ with increasing P_t is evidence for the presence of $q\bar{q}g$ contributions in the final state.

5 Event selection and final state reconstruction

The DIS event sample used in this analysis was obtained from data collected during the 1994 HERA operation, and corresponds to an integrated luminosity of about 2 pb^{-1}. The event trigger required a minimum energy deposition in the BEMC of 4 GeV. The events were selected according to the kinematical properties of the scattered electron [5] [32] and the hadronic final state. The following variables are used:

$$Q^2 = 4E_e E_{e'} \cos^2(\theta_{e'}/2) \qquad y_e = 1 - E_{e'}/E_e \sin^2(\theta_{e'}/2) \qquad x = Q^2/(y_e s),$$

calculated from the electron beam energy $E_e (= 27.5$ GeV$)$, the energy $E_{e'}$ and the polar angle $\theta_{e'}$ of the scattered electron, and $\sqrt{s}$, the invariant ep mass. The invariant mass M_X of the hadronic system X is calculated as a geometric mean :

$$M_X^2 = M_X(e)\ M_X(h) \tag{1}$$

with

$$M_X^2(e) = [E_e - P_{z,e} - (E_{e'} - P_{z,e'})](E_h + P_{z,h}) - P_{x,h}^2 - P_{y,h}^2$$

$$M_X^2(h) = E_h^2 - P_{z,h}^2 - P_{x,h}^2 - P_{y,h}^2$$

where

$$E_h = \textstyle\sum_{hadrons} E_i \qquad P_{x(y,z),h} = \textstyle\sum_{hadrons} P_{x(y,z),i}$$

[5]The data analysed here were taken with a positron beam in HERA. The term electron is generic.

and E_i, $P_{x,i}$, $P_{y,i}$, $P_{z,i}$ are the individual energy and momentum components of the hadronic final state in the laboratory system.

The hadron 4-momenta were calculated using the interaction vertex and the energy deposit clusters in the calorimeters. In addition the momentum from each reconstructed track was included up to a maximum of 350 MeV, i.e. for tracks with $P < 350$ MeV the momentum as measured and for tracks with $P > 350$ MeV only 350 MeV were taken. This is to compensate for losses in the calorimetric measurement of charged hadrons. The value of 350 MeV was determined by the requirement of a balance between $P_{t,e'}$, the transverse momentum of the scattered electron, and $P_{t,h}$, the transverse momentum of the observed hadrons. For the LRG events, which have only very small unobserved p_t contributions in the forward direction, this procedure yields a width of 1.2 GeV in the $P_{t,h} - P_{t,e'}$ distribution.

The reconstruction errors for $M_X(e)$ and $M_X(h)$ are mostly independent. Large errors can occur because of initial state QED radiation $[M_X(e)]$ or from acceptance losses in the backward direction $[M_X(h)]$. Studies with simulated events show that using the geometric mean [equ.(1)] reduces extreme deviations from the true M_X.

From the above quantities and with q the 4-momentum of γ^* the variables β and $x_{I\!P}$ can be calculated as follows

$$\beta = \frac{-q^2}{2q\cdot(p-Y)} = \frac{Q^2}{Q^2+M_X^2-t}$$

$$x_{I\!P} = \frac{q\cdot(p-Y)}{q\cdot p} = \frac{Q^2+M_X^2-t}{Q^2+W^2-M_p^2} = \frac{x}{\beta}.$$

In the "proton infinite momentum frame", the variable $x_{I\!P}$ can be interpreted as the fraction of the proton momentum transferred to the photon by the exchanged $I\!P$, while β is the fraction of the $I\!P$ momentum carried by the parton coupling to the photon.

The 4-momentum transfer squared, t, between the incident proton and the final state Y is small in LRG events since the forward detector selection amounts to $|t| < 1$ GeV^2. Therefore t, which is not measured, can be neglected in the above formulae.

The following selection criteria were applied to the scattered electrons of the LRG sample:

1. The electron energy was constrained to be large ($E_{e'} > 14.4$ GeV) by requiring $y_e < 0.5$. This keeps the photoproduction background at a negligible level, and removes events where the hadronic system X is boosted strongly towards the BEMC and the backward beam pipe hole.
2. The electron scattering angle was limited to $156° < \theta_{e'} < 173°$ to avoid events with electron energy deposition near the edges of the BEMC.
3. Q^2 was required to be in the range 10 to 100 GeV^2. In this Q^2 range there is almost constant acceptance for electrons.

Further selections were made with quantities derived from the full final state:

1. The interaction vertex was required to be within ±30 cm of its nominal position and to be reconstructed with at least 1 track in the central jet chamber.
2. $x_{I\!P} < 0.05$ was required to suppress non-diffractive contributions.

3. The largest rapidity gap was required to include the pseudorapidity range of the forward detectors (see section 2) by demanding the absence of significant activity in these detectors and, for $\eta > 3.2$, in the LAr calorimeter. These requirements have a high efficiency to reject events with particles in the region $7.5 > \eta > 3.2$ [33].

4. The mass M_X of the hadronic final state was required to be bigger than 4 GeV, the approximate limit below which the thrust axis ceases to be correlated with a 2-parton axis.

5. $M_X < 36$ GeV was required to avoid events where the rapidity gap requirement implies an acceptance below 25%.

With these selection criteria 6865 events were collected in the M_X range from 4 to 36 GeV. They are distributed over the M_X intervals as shown in Table 1. These events cover the range $10^{-4} < x < 3.2 \cdot 10^{-2}$, and $30 < W < 210$ GeV.

	M_X intervals (GeV)						
	4-6	6-8	8-11	11-15	15-19	19-24	24-36
No. of events	1439	1278	1404	1130	711	502	401

Table 1: Number of observed events per measured M_X interval.

6 Corrections for resolution and acceptance

Using simulated events, the measured distributions have been corrected for detector resolution and acceptance losses to give cross sections in a kinematic range defined by

$$M_Y < 1.6 \text{ GeV}, \; x_{\mathbb{P}} < 0.05, \; |t| < 1 \text{ GeV}^2, \; 10 < Q^2 < 100 \text{ GeV}^2 \text{ and } \; y < 0.5, \qquad (2)$$

for the same M_X intervals as given in Table 1. Events with these M_Y, $x_{\mathbb{P}}$ and t limits have large rapidity gaps in the detector for kinematic reasons [3]. This cross section definition only allows for small non-diffractive contributions, which are typically less than 10% [20], and it avoids the need for a statistical subtraction from the data of a model-dependent non-diffractive background. It also reduces the systematic error due to model dependence of acceptance corrections.

Two different Monte Carlo event simulations were used to correct the observed experimental distributions. These were RAPGAP in the ME+PS and in the AR+CD mode, but with simple (flat) quark and gluon distribution functions for the pomeron and without Q^2 evolution. The generated events were passed through a full detector simulation and had the same event reconstruction as real data. The Monte Carlo simulation of this simplified model described quite well the kinematic distributions of $Q^2, x_{\mathbb{P}}$ and W, and further variables describing the detector response. The observed P_t distributions were described qualitatively. With an additional smooth weighting function for the generated events, which depends on thrust jet P_t at the hadron level, the P_t distributions in all M_X intervals were very well approximated over the full P_t range. The measured thrust distribution is also well reproduced after the weighting in P_t, as shown in Fig. 3.

The contents of the 2-dimensional bins of the experimental (P_t^2, M_X) and (T, M_X) distributions were multiplied by the ratios of the numbers of generated to reconstructed and selected events in the corresponding intervals for the MC distributions.

Monte Carlo studies show that the thrust jet P_t is resolved to better than 1 GeV. The correction factors vary only slowly from bin to bin in all P_t^2 distributions and are large (> 2) only for masses $M_X > 15$ GeV and for $P_t^2 < 1$ GeV^2. In the thrust distributions, the correction

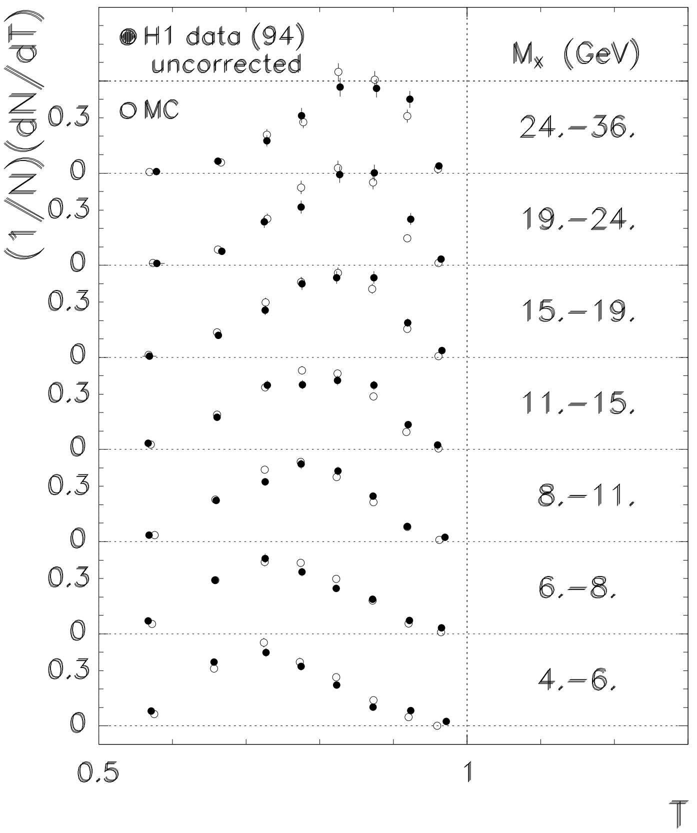

Figure 3: Normalized, uncorrected thrust distribution, with N the number of observed events, for data (full points) and the simplified, P_t-weighted MC simulation (open points), as described in the text.

factors in each mass bin vary less than a factor two, except for the lowest and the highest thrust bins. Since those intervals contain only a very small fraction of the events (see Fig. 3), these factors have very little influence on the average thrust value. The corrected average thrust is calculated from the corrected thrust distribution.

To estimate the systematic errors, the following contributions were taken into account:

- uncertainty in the LAr hadronic energy scale;
- uncertainty in the BEMC hadronic and electromagnetic energy scales;
- uncertainty in the correction factors due to freedom in the P_t weighting;
- differences between event generation schemes (parton shower, colour dipole).

The two latter contributions were the largest sources of systematic error. Their effect was determined for each data point from the differences between the four correction factors coming from the two event generation schemes - with colour dipole radiation or with parton showers - and each of them in the unweighted and the weighted mode. The unweighted P_t distributions at detector level of the simulated events were slightly flatter than the data, and the weighted ones were slightly steeper.

Radiative corrections have been applied using the programs HERACLES [34] and RAPGAP in the matrix element and ARIADNE modes, as described in Section 3. The corrections are smaller than the statistical errors for all data points shown.

The statistical, and the statistical and systematic errors added in quadrature, are indicated in the figures as the inner and the outer error bars, respectively. Systematic and statistical errors are given separately in the respective tables.

7 Results

7.1 Correlation of thrust with M_X, P_t and Q^2

In Fig. 4a thrust is shown as a function of $1/M_X$, averaged in seven M_X intervals (see Table 2) in the range 4 to 36 GeV, and averaged over the kinematic region of equ.(2). The same data are also given in Table 2. The correlation of thrust with $1/M_X$ rather than M_X is shown because it

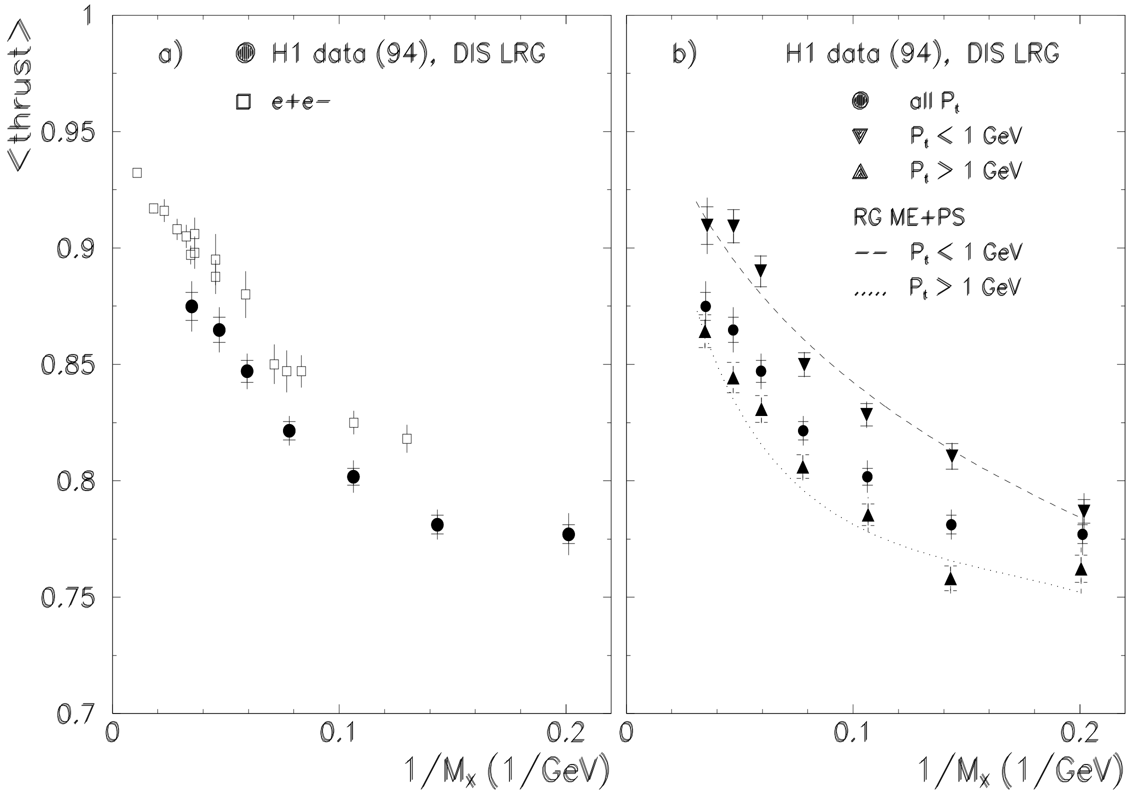

Figure 4a: (a) Average thrust $\langle T\rangle$, as a function of $1/M_X$ for LRG data, and for e^+e^- annihilation data [17, 35] as a function of $1/\sqrt{s_{ee}}$; **4b:** Average thrust $\langle T\rangle$, as a function of $1/M_X$, for all events, for events with $P_t < 1$ GeV and for events with $P_t > 1$ GeV, with predictions from RAPGAP (see text). The data points are given at $1/\langle M_X\rangle$.

allows perturbative and hadronization effects on thrust to be distinguished in a simple manner. For $M_X \to \infty$ the latter should become negligible. For comparison, Fig. 4a includes the available data for thrust in e^+e^- annihilation events [17, 35] plotted at $M_X = \sqrt{s_{ee}}$. The following features are noteworthy:

1. $\langle T\rangle$ increases with M_X. It is also observed in these data that the particle multiplicity (not shown here) also increases with M_X. This implies that the final state is not isotropic, since in that case $\langle T\rangle$ would fall, and approach 0.5, as $1/M_X \to 0$. The growth of $\langle T\rangle$ signifies an increasing back-to-back correlation of the momentum flow as the final state mass increases. Hence, the thrust direction corresponds to an effective topological axis of the event. This feature rules out

$\langle M_X \rangle$(GeV)	$\langle T \rangle$	stat.error	syst.error	B
4.97	0.777	0.004	0.008	0.18
6.98	0.781	0.004	0.005	0.16
9.40	0.802	0.004	0.006	0.18
12.81	0.822	0.004	0.005	0.16
16.82	0.847	0.005	0.006	0.12
21.20	0.865	0.005	0.008	0.10
28.64	0.875	0.006	0.009	0.10

Table 2: Mean thrust values as a function of $\langle M_X \rangle$. The following bin limits for M_X were used: 4, 6, 8, 11, 15, 19, 24, 36 GeV. To combine values of $\langle T \rangle$ from different M_X intervals, the relative cross section weights B are to be used.

fireball type models [36] with isotropic configurations of final state hadrons in virtual photon diffractive dissociation. Similar effects have also been observed in hadronic single diffractive dissociation [37].

2. There is a striking similarity between the $\sqrt{s_{ee}}$ dependence of $\langle T \rangle$ in e^+e^- annihilation and its M_X dependence in virtual photon dissociation, for the kinematical range of this analysis. The slopes are comparable, but $\langle T \rangle$ of DIS LRG events is lower by an approximately constant value of 0.025. This similarity is not so evident in [21].

For $4 < M_X < 36$ GeV the thrust-mass correlation may be described by

$$\langle T \rangle = T_\infty - H/M_X + F/M_X^2, \tag{3}$$

as first observed in e^+e^- annihilation experiments [17]. There T_∞ is related to thrust at the parton level and hence to α_s [38] in the s_{ee} range of the data. The coefficient H describes the contribution to thrust of jet broadening by hadronization. Such a power correction term was theoretically predicted [38], confirmed by data [17], reproduced with simulated events using limited p_t hadronization [39] and is now discussed in the context of non-pertubative QCD [40]. Contrary to the situation in e^+e^- annihilation, a theoretical justification of the T_∞ and the $1/M_X$ terms has not yet been given for LRG events, but the data suggest that equ.(3) applies here also. The $1/M_X^2$ term is an ansatz to account for a bias of thrust towards large values when such a maximum search method is applied to low particle multiplicity final states which occur at low M_X. In a fit of this parameterization to the M_X range of the LRG data the parameter T_∞ is correlated strongly with H and F. To express the measured $\langle T \rangle$ dependence on M_X with minimally correlated parameters an expansion of $\langle T \rangle$ in $1/M_X$ at a mass $M_X = M_0$ inside the data range is appropriate:

$$\langle T \rangle = T_0 - H \cdot (1/M_X - 1/M_0) + F \cdot (1/M_X^2 - 1/M_0^2) \tag{4}$$

Here T_0 is $\langle T \rangle$ at $M_X = M_0$. In a fit, with $M_0 = 20$ GeV, the coefficient F for the e^+e^-

Data	T_0 at $M_X = 20$ GeV	H (GeV)
ep DIS LRG	0.857 ± 0.003	1.78 ± 0.03
e^+e^- annihilation	0.881 ± 0.002	1.72 ± 0.05

Table 3: Results from the $T - M_X$ correlation (eqn. 2) fitted to this data and to e^+e^- data [17, 35], in the range from $6 < M_X < 36$ GeV. T_0 is the value of $\langle T \rangle$ at $M_X = 20$ GeV, and H the coefficient of the hadronization ($1/M_X$) term. The errors given are statistical errors for the ep data and statistical and systematic errors combined for the e^+e^- data. For the ep data T_0 has in addition a systematic error of ± 0.006. The H values for ep and e^+e^- have in addition a common error of 0.11 from their correlation to the uncertainty in the low multiplicity fluctuation term F.

annihilation data was poorly constrained and was thus fixed to the result found in LRG events

($F = 5.0 \pm 0.6$ GeV^2). The results of the fits in Table 3 show that the power corrections (H) are compatible, while the thrust values are significantly lower in LRG than in e^+e^- events.

The result $\langle T\rangle_{LRG} < \langle T\rangle_{ee}$ means that the final state in DIS LRG events cannot be understood as a simple $q\bar{q}$ state with standard limited p_t hadronization [39]. It implies that higher parton multiplicities are even more important in DIS LRG events than in e^+e^- annihilation. For a $q\bar{q}$ parton configuration, $\langle T\rangle_{LRG}$ can only be less than $\langle T\rangle_{ee}$ if the power corrections are stronger than in e^+e^-annihilation data. Then the value of H would have to be larger than found in this fit. A quantitative interpretation of the difference $\langle T\rangle_{LRG} - \langle T\rangle_{ee}$ in the PD picture in terms of contributions from the Born-term, and from the QCD-Compton and BGF subprocesses (see Fig. 2), requires a treatment of the non-perturbative diffractive vertex in these diagrams. This is not yet available. In the IMF picture, the expressions for $\langle T\rangle_{LRG}$ are divergent.

Contributions from underlying configurations with three, as in Fig. 2b, c and d, or more partons can also be studied using the correlation between P_t and thrust. In Fig. 4b we show $\langle T\rangle$ for events with P_t smaller and larger than 1 GeV. At each M_X point average thrust for large P_t is lower than for small P_t, demonstrating the presence of configurations with at least 3 (non-collinear) partons. The observed difference of $\langle T\rangle$ cannot be attributed to the selection of events with different hadronization properties. If this were the case, the difference would have to be proportional to $1/M_X$, and this is not compatible with the data. On the contrary, the difference is compatible with a higher, M_X independent, parton multiplicity. Monte Carlo studies confirm that this P_t dependent $\langle T\rangle$ behaviour is that expected with 3-parton configurations, as seen in the curves in Fig. 4b, which show RAPGAP (ME+PS) expectations for a mixture of $q\bar{q}$ and $q\bar{q}g$ configurations.

The dependence of $\langle T\rangle$ on Q^2 was also studied. The value of $\langle T\rangle$ changes by no more than ± 0.01 over the Q^2 range 10 to 100 GeV^2. Since $\langle M_X\rangle$ is found to be independent of Q^2, it can be concluded that the data show almost no correlation between thrust and Q^2.

7.2 $\mathbf{P_t^2}$ distributions

The cross sections differential in P_t^2 are shown in Fig. 5a and in Table 4, for six M_X intervals in the mass range from 6 to 36 GeV, and normalized to unity in each M_X interval. The M_X interval from 4 to 6 GeV is not included since the flattening of $\langle T\rangle$ with $1/M_X$ in Fig. 4a, indicates that effects from low multiplicity fluctuations are becoming strong. For each M_X interval the data are displayed only in those bins of P_t^2 that are kinematically fully accessible. In Fig. 5b the P_t^2 distribution of one mass range ($19 < M_X < 24$ GeV) is displayed on a linear scale in P_t^2. The data show:

1. a steep rise of the distribution towards low P_t^2 values, demonstrating a dominant alignment of the final state thrust axis with the initial $\gamma^* p$ collision direction;

2. a shape of the P_t^2 distributions nearly independent of M_X, suggesting the factorizable form
$$\mathrm{d}\sigma(M_X, P_t^2)/\mathrm{d}P_t^2 = A(M_X) \cdot B(P_t^2); \qquad (5)$$

3. a substantial high P_t^2 tail.

The large high-P_t tail supports the conclusion in Sect. 7.1 that there are significant contributions from parton multiplicities higher than $q\bar{q}$, such as those shown in Figs. 2b-d. The same conclusion may be gained from Fig. 6 where the fractions of events with P_t^2 values above 1.0 GeV^2 and above 3.0 GeV^2, respectively, are displayed as a function of M_X. The fraction at the lowest M_X point in Fig. 6b is relatively low because of the reduced phase space for $P_t^2 > 3$ GeV^2 here (see Table 4). For higher masses the fractions reach about 64% for $P_t^2 > 1$ GeV^2 and 35% for $P_t^2 > 3$ GeV^2. The model predictions indicate that such large values of P_t^2 require hard processes, which involve more than two final state partons, to play an important role in DIS LRG events.

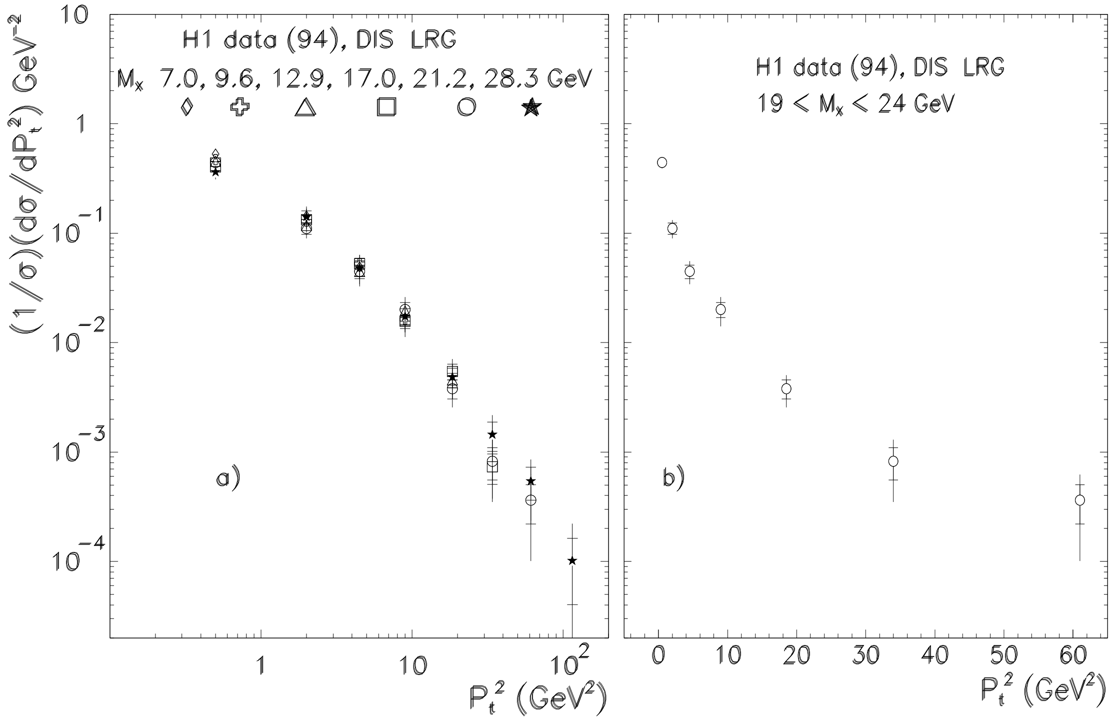

Figure 5a: Normalized thrust jet P_t^2 distributions for six M_X intervals. The P_t^2 bin limits are 0, 1, 3, 6, 12, 25, 43, 79, and 151 GeV^2; **5b:** Normalized thrust jet P_t^2 distribution for $19 < M_X < 24$ GeV with a linear P_t^2 scale.

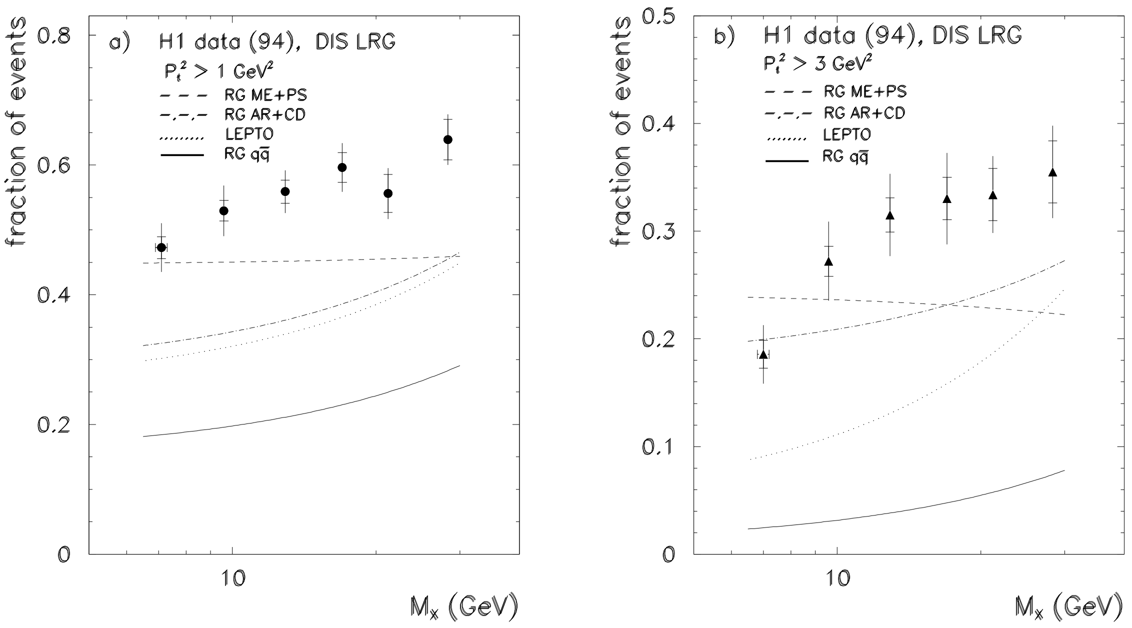

Figure 6a: Fraction of events with $P_t^2 > 1$ GeV^2 for six M_X intervals, together with four model predictions (see text); **6b:** as in a, but with $P_t^2 > 3$ GeV^2.

8 Comparison with models

The GVDM model in combination with quasi-elastic diffractive vector meson proton scattering [16] leads to final states X with spin $J = 1$. For such a situation the width of the P_t^2

$\langle P_t^2 \rangle$ GeV^2	$\langle M_X \rangle$ (GeV)	$(1/\sigma)(d\sigma/dP_t^2)$ GeV^{-2}	stat.error	syst.error
0.37	6.96	0.527	0.018	0.038
1.88	6.96	0.144	0.009	0.022
4.21	7.10	0.042	0.004	0.007
0.38	9.39	0.470	0.017	0.039
1.84	9.36	0.129	0.008	0.022
4.30	9.31	0.052	0.004	0.007
8.38	9.54	0.016	0.002	0.003
0.40	12.72	0.451	0.019	0.033
1.83	12.74	0.117	0.009	0.013
4.22	12.77	0.045	0.004	0.005
8.54	12.78	0.019	0.002	0.003
15.97	13.10	0.0051	0.0007	0.0013
0.41	16.90	0.404	0.024	0.038
1.79	16.78	0.133	0.012	0.016
4.32	16.70	0.053	0.006	0.008
8.47	16.98	0.016	0.002	0.004
17.10	16.89	0.005	0.001	0.001
30.75	16.85	0.0007	0.0002	0.0003
0.37	21.01	0.444	0.030	0.044
1.84	21.10	0.111	0.013	0.016
4.22	21.40	0.045	0.006	0.009
8.08	20.91	0.020	0.003	0.005
16.19	21.07	0.0038	0.0008	0.001
33.18	20.79	0.0008	0.0003	0.0004
51.70	22.15	0.00039	0.00014	0.00022
0.41	27.79	0.361	0.032	0.039
1.83	28.05	0.141	0.018	0.028
4.26	27.94	0.048	0.008	0.013
8.42	28.26	0.017	0.003	0.004
17.38	28.65	0.0049	0.0010	0.0011
32.09	29.35	0.0014	0.0004	0.0006
58.28	28.18	0.00054	0.00018	0.00025
113.20	30.45	0.00011	0.00006	0.00011

Table 4: The $(1/\sigma)(d\sigma/dP_t^2)$ distribution. The following bin limits were used: 0, 1, 3, 6, 12, 25, 43, 79, 151 GeV^2 for P_t^2, and 6, 8, 11, 15, 19, 24, 36 GeV for M_X. The table gives the mean values of P_t^2 and M_X in each 2-dimensional bin, the differential cross section in this bin divided by the total cross section for the respective M_X bin, and the statistical and the systematic errors in the same normalized units. The weight factors from Table 2 are to be applied to combine distributions from different mass bins.

distribution is proportional to M_X^2. Within present statistics the data do not support such a contribution. Thus the spin parity structure of X is neither pure nor dominantly vector.

The SCI model as presently implemented in LEPTO reproduces the M_X dependence of $\langle T \rangle$ as shown in Fig. 7, but fails to describe the fractions of events with P_t^2 larger than 1 or 3 GeV^2 (Fig. 6). This model as proposed has no means with which to adjust this prediction and therefore it cannot describe the LRG events exclusively.

The PD picture is qualitatively consistent with two independent features of the data. Firstly, the strong, M_X independent, alignment peak seen in Fig. 5 is expected because of colour transparency. Secondly, the cross section ratio for $q\bar{q}g$ to $q\bar{q}$ configurations is expected to be larger than in e^+e^- annihilation, mainly because of the large contribution for the BGF process, again

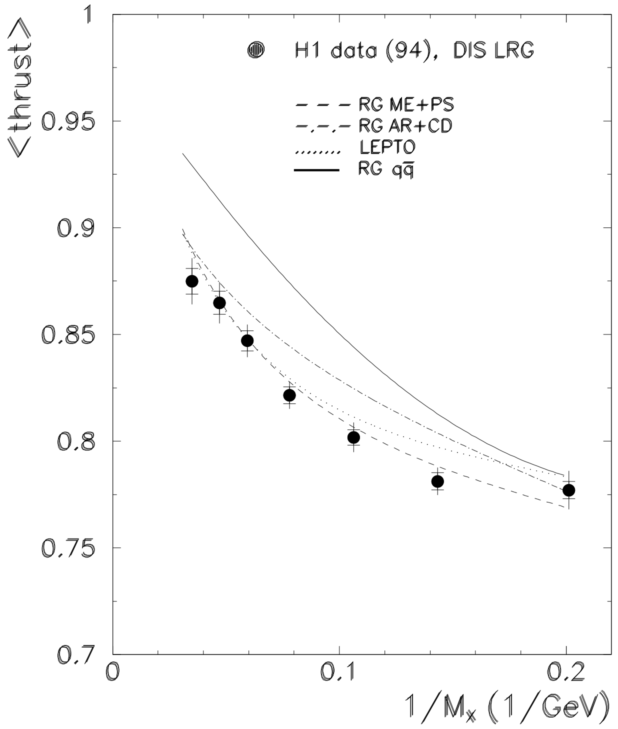

Figure 7: Comparison of model predictions (see text) with the M_X dependence of $\langle T \rangle$.

as a consequence of colour transparency. This is supported by the observation of $\langle T \rangle_{LRG} < \langle T \rangle_{ee}$ in Fig. 4a, and by the large P_t^2 tail in Fig. 5. The qualitative expectations are confirmed by calculations in limited regions of phase space [9].

Calculations of the IMF picture in the RAPGAP implementation are shown in Figs. 6 and 7. The AR+CD mode, which does not employ matrix elements for the QCD-C process, systematically predicts thrust too high and fractions of events with large P_t too low. The ME+PS predictions are closer than those for the AR+CD mode, but the agreement with the data is not completely satisfactory. There are, however, several means to adjust the RAPGAP predictions to the data. One is a modification of the $\hat{p}_t$ cut-off scheme. The present scheme, with an M_X independent $\hat{p}_t$ cut-off value, is responsible for the counter-intuitive behaviour of the prediction for the M_X dependence of the large P_t event fractions in the ME+PS mode. In view of these model implementation problems, one cannot conclude that this approach is unable to describe the data.

The RG q$\bar{\text{q}}$ curves, which approximate the simple AJM, indicate the extent to which the virtual photon dissociation process to $q\bar{q}$ only is unable to describe the data.

9 Summary and conclusions

A thrust analysis of DIS large rapidity gap (LRG) events, that is of events attributable to the process $\gamma^* p \to XY$, with $M_X > 4$ GeV, $M_Y < 1.6$ GeV, $x_{I\!P} < 0.05$ and $10 < Q^2 < 100$ GeV^2 reveals:

- a dominant two-jet topology of the final state X;

- a clear alignment of the thrust axis with the incoming proton direction in the X rest frame;
- a dependence of the average thrust value $\langle T\rangle$ on P_t, the thrust jet momentum transverse to the incoming proton direction: $\langle T\rangle$ decreases when P_t increases;
- a P_t^2 spectrum independent of M_X;
- a sizeable fraction of events with large P_t^2 (> 3 GeV^2);

and in comparison with e^+e^- :

- the influence of hadronization on $\langle T\rangle$ is compatible with e^+e^- ;
- $\langle T\rangle$ is smaller than in e^+e^- at $M_X = \sqrt{s_{ee}}$.

These features together cannot be explained by a pure $q\bar{q}$ configuration. It has been shown in a model independent way that a substantial contribution of $q\bar{q}g$ and higher multiplicity parton configurations is required in the final state X. This contribution is greater than in e^+e^- annihilation data.

There are two equivalent pictures for diffractive LRG event production. In the first the virtual photon fluctuates into multi-parton states together with quasi-elastic parton-proton diffraction. In the second the electron scatters off partons which constitute the diffractive exchange. The expectations of both pictures are broadly in agreement with the results of this analysis. Two other mechanisms for LRG event production, GVDM in the particular combination with quasi-elastic vector meson proton diffraction, and non-diffractive ep DIS plus subsequent soft colour interaction, do not explain all topological properties of the observed events.

The abundance of parton multiplicities higher than $q\bar{q}$ implied by topological event properties is consistent with the large gluon content in diffractive exchange found in QCD-fits to the inclusive production cross section of DIS LRG events [20].

10 Acknowledgements

We are grateful to the HERA machine group whose outstanding efforts have made and continue to make this experiment possible.

We thank the engineers and technicians for their work in constructing and now maintaining the H1 detector, our funding agencies for financial support, the DESY technical staff for continual assistance, and the DESY directorate for the hospitality which they extend to the non-DESY members of the collaboration.

References

[1] ZEUS Collab., M. Derrick et al., Phys. Lett. B315 (1993) 481.

[2] H1 Collab., T. Ahmed et al., Nucl. Phys. B429 (1994) 477.

[3] H1 Collab., T. Ahmed et al., Phys. Lett. B348 (1995) 681.

[4] ZEUS Collab., M. Derrick et al., Z. Phys. C68 (1995) 569.

[5] M.L. Good and W.D. Walker, Phys. Rev. 120 (1960) 1857.

[6] J.D. Bjorken and J.B. Kogut, Phys. Rev. D8 (1973) 1341.

[7] N.N. Nikolaev and B.G. Zakharov, Z. Phys. C49 (1991) 607, Z.Phys. C53 (1992) 331, Z. Phys. C64 (1994) 607;
E. Levin and M. Wüsthoff, Phys. Rev. D50 (1994) 4306;
A. Berera and D.E. Soper, Phys. Rev. D53 (1996) 6162;
S.J. Brodsky, A. Hebecker, and E. Quack, Phys. Rev. D55 (1997) 2584;
S.J. Brodsky, P. Hoyer, and L. Magnea, Phys. Rev. D55 (1997) 5585.

[8] W. Buchmüller and A. Hebecker, Phys. Lett. B355 (1995) 573.

[9] W. Buchmüller, M.F. McDermott, and A. Hebecker, Nucl. Phys. B487 (1997) 283, "High-Pt Jets in Diffractive Electroproduction", preprint DESY 97-099, hep-ph/9706354.

[10] G. Ingelman and P.E. Schlein, Phys. Lett. B152 (1985) 256.

[11] A.B. Zamolodchikov, B.Z. Kopeliovich, and L.I. Lapidus, Pisma v. ZhETF 33 (1981) 612;
G. Bertsch et al., Phys. Rev. Lett 47 (1981) 267.

[12] L. Frankfurt and M. Strikman, Phys. Rep. 160 (1988) 235.

[13] A. Edin, G. Ingelman, and J. Rathsman, Phys. Lett. B366 (1996) 371.

[14] J.J. Sakurai and D. Schildknecht, Phys. Lett. B40 (1972) 121;
B. Gorczyca and D. Schildknecht, Phys. Lett. B47 (1973) 71;

[15] L. Stodolsky, Phys. Lett. B325 (1994) 505.

[16] D. Schildknecht and H. Spiesberger, "Generalized Vector Meson Dominance and low x inelastic electron-proton scattering", preprint BI-TP 97/25, hep-ph/9707447.

[17] PLUTO Collab., Ch. Berger et al., Z. Phys. C12 (1982) 297.

[18] S. Brandt et al., Phys. Lett. 12 (1964) 57.

[19] E. Farhi, Phys. Rev. Lett. 39 (1977) 1587.

[20] H1 Collab., C. Adloff et al., "Inclusive Measurement of Diffractive Deep-inelastic ep Scattering", DESY 97-158, subm. to Z. Phys. C.

[21] ZEUS Collab., J. Breitweg et al., "Event shape analysis of deep inelastic scattering events with a large rapidity gap at HERA", DESY 97-202.

[22] H1 Collab., I. Abt et al., Nucl. Instr. and Meth. A386 (1997) 310 and Nucl. Instr. and Meth. A386 (1997) 348.

[23] H1 BEMC Group, J. Ban et al., Nucl. Instr. and Meth. A372 (1996) 399.

[24] H. Jung, Comp. Phys. Comm. 86 (1995) 147;
H. Jung, "Modelling Diffractive Processes", Topical Conference on Hard Diffractive Processes, Eilat, Israel, Febr. 1996, p. 406.

[25] Yu.L. Dokshitzer, JETP 46 (1997) 641;
V.N. Gribov, L.N. Lipatov, Sov. Journ. Nucl. Phys. 15 (1972) 78:
G. Altarelli, G. Parisi, Nucl. Phys. B126 (1977) 298.

[26] P.R. Newman, "Inclusive Measurements of Diffraction in Deep Inelastic Scattering and Photoproduction", DESY - 96-162A, Int. Workshop on Deep Inelastic Scattering and Related Phenomena, Rome, Italy, Apr. 1996;
J. Phillips,"Diffractive Hard Interactions in Electron Proton Collisions", Proc. XXVIII Int. Conf. on High Energy Physics, Warsaw, Poland, July 1996.
H1 Collab. "A measurement and QCD Analysis of the Diffractive Structure Function $F_2^{D(3)}$", paper pa02-061 submitted to the XXVIII Int. Conf. on High Energy Physics, Warsaw, Poland, July 1996.

[27] M. Glück, E. Reya, and A. Vogt, Z. Phys. C53 (1992) 651.

[28] ARIADNE 4.08, L. Lönnblad, Comput. Phys. Comm. 71 (1992) 15.

[29] G. Gustafson and U. Petterson, Nucl. Phys. B306 (1988) 746;
B. Andersson et al., Z. Phys. C43 (1989) 625.

[30] JETSET 7.3 and 7.4, T. Sjöstrand, Comput. Phys. Com. 82 (1994) 74.

[31] G. Ingelman, A. Edin, and J. Rathsman, "LEPTO 6.5 - A Monte Carlo Generator for Deep Inelastic Lepton-Nucleon Scattering", DESY 96-057.

[32] H1 Collab., S. Aid et al., Nucl. Phys. B470 (1996) 3.

[33] A. Mehta, "Measurement of the Diffractive Proton Structure Function and Calibration of the Forward Muon Detector at H1", PhD thesis (University of Manchester), 1994 (Unpublished).

[34] HERACLES 4.4, A. Kwiatkowski, H. Spiesberger, and H.-J. Möhring, Comput. Phys. Commun. 69 (1992) 155.

[35] MARK II Collab., A. Peterson et al., Phys. Rev. D37 (1988) 1;
TASSO Collab., W. Braunschweig et al., Z. Phys. C45 (1989) 11 and Z. Phys. C47 (1990) 187;
AMY Collab., Y.K. Li et al., Phys. Rev. D41 (1990) 2675;
DELPHI Collab., P. Abreu et al., Z. Phys. C73 (1997) 229.

[36] R. Hwa, Phys. Rev. Lett. 26 (1971) 1143;
M. Jacob and R. Slansky, Phys. Rev. D5 (1972) 1847.

[37] UA4 Collab., D. Barnard et al., Phys. Lett. B166 (1986) 459;
UA5 Collab., R.E. Ansorge et al., Z. Phys. C33 (1986) 175;
NA22 Collab., M. Adamus et al., Z. Phys. C39 (1988) 301.

[38] A. de Rujula et al., Nucl. Phys. B138 (1978) 387.

[39] R.D. Field and R.P. Feynman, Nucl. Phys. B136 (1978) 1.

[40] B.R. Webber, Phys. Lett. B339 (1994) 148;
Yu. L. Dokshitzer and B.R. Webber, Phys. Lett. B352 (1995) 451;
R. Akhoury, V.I. Zakharov, Phys. Lett. B357 (1995) 646;
Yu. L. Dokshitzer, G. Marchesini, and B.R. Webber, Nucl. Phys. B469 (1996) 451;
P. Nason and M.H. Seymour, Nucl. Phys. B454 (1995) 291.